

milliFlow: Scene Flow Estimation on mmWave Radar Point Cloud for Human Motion Sensing

Fangqiang Ding¹, Zhen Luo¹, Peijun Zhao², Chris Xiaoxuan Lu^{1,*}

¹ University of Edinburgh, Edinburgh, Scotland, United Kingdom

² Massachusetts Institute of Technology, Cambridge, Massachusetts, USA

ABSTRACT

Approaching the era of ubiquitous computing, human motion sensing plays a crucial role in smart systems for decision making, user interaction, and personalized services. Extensive research has been conducted on human tracking, pose estimation, gesture recognition, and activity recognition, which are predominantly based on cameras in traditional methods. However, the intrusive nature of cameras limits their use in smart home applications. To address this, mmWave radars have gained popularity due to their privacy-friendly features. In this work, we propose *milliFlow*, a novel deep learning method for scene flow estimation as a complementary motion information for mmWave point cloud, serving as an intermediate level of features and directly benefiting downstream human motion sensing tasks. Experimental results demonstrate the superior performance of our method with an average 3D endpoint error of 4.6cm, significantly surpassing the competing approaches. Furthermore, by incorporating scene flow information, we achieve remarkable improvements in human activity recognition, human parsing, and human body part tracking. To foster further research in this area, we provide our codebase and dataset for open access¹.

1 INTRODUCTION

Perceiving and understanding human behaviours play a pivotal role in human-centred applications such as disaster response [45, 57], surveillance [8, 48] and health monitoring [18, 47]. Conventional methods rely on cameras [25, 55] or wearables [37, 62] which are prone to visual deterioration (such as low lighting conditions, smoke, and fog) and raise privacy concerns, potentially compromising user experience with intrusive measures. To address these concerns, researchers, on the other side, also propose to use wireless radio frequency (RF) signals bounced off the human body for human sensing [34, 59] which is robust against poor lighting, privacy-preserving and non-intrusive to users. Among many RF techniques, single-chip millimeter wave (mmWave) radar emerges as a low-cost sensor that can provide more trustworthy point clouds of a scene under environment dynamics due to its transceiver design and the usage of Frequency

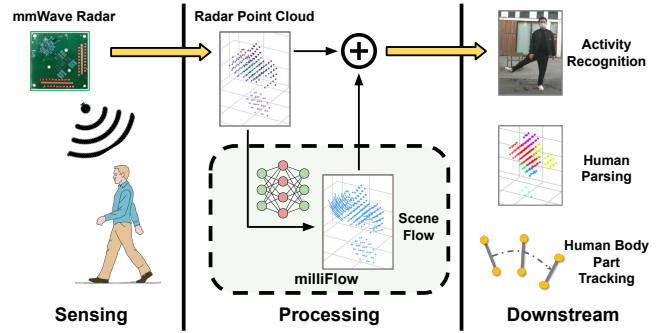


Figure 1: We propose *milliFlow*, a scene flow estimation module to provide an additional layer of point-wise motion information on top of the original mmWave radar point cloud in the conventional radar human motion sensing pipeline.

Modulated Continuous Wave (FMCW). For these reasons, there has been a significant increase in the production of single-chip radars [2] and wide deployment in real-world scenarios, ranging from smart buildings [5, 60] to vehicle cabins [14, 54], and to first-responder toolkits [3].

As motion is naturally continuous and human bodies are non-rigid, point-wise velocity per radar frame is intuitively a strong cue for improving the motion estimation robustness and has been widely used in prior arts [36, 56, 65, 73]. However, fine-grained velocity is difficult to obtain when it comes to mmWave radars. First, while some radars provide the Doppler velocity of a point, the velocity resolution is rather low ($>0.15\text{m/s}$) that cannot accurately capture the human body movement, which is usually slower than 0.5m/s in domestic life. Moreover, mmWave radar only senses radial Doppler information but fails to capture the tangential one. For some radars designed for human sensing, e.g., the Vayyar radar [4] used in this work, the Doppler information is even absent in their sensor outputs. Second, extracting motion information from consecutive mmWave radar point clouds is also highly error-prone due to limitations inherent in low-cost single-chip mmWave radar. These limitations include extremely sparse point clouds due to the constant false alarm rate (CFAR) algorithm [53] used on-chip and the presence of ghost points caused by multi-path effect [23]. More recently, it has been found that in a single radar frame, only a subset

¹ommitted for blind review.

of body parts reflecting the signal towards the radar can be observed, while other parts deflecting the signal away from the radar are missing from the capture [12]. As a result, some human body parts detected in one frame may disappear in the next frame. For the above reasons, conventional tracking methods struggle to track human motion across frames or give fine-grained velocity in between.

In this work, we propose to estimate and use scene flow as intermediate features to better support radar-based human sensing. Scene flow refers to a set of displacement vectors between two consecutive point-cloud frames describing the motion field of a 3D scene. We hypothesise that scene flow, if estimated accurately, is able to drastically facilitate cross-frame movement analysis by directly exposing per-point motion features, thereby addressing the aforementioned challenges in previous research. Scene flow has long been proven very effective by the computer vision community in image-based human motion sensing applications [29, 42, 64]. However, estimating scene flow on mmWave radar point cloud is non-trivial because of the inherent sparsity and noise of radar point cloud. Directly applying conventional scene flow estimation methods designed for LiDAR or RGB-D cameras [15, 35, 69, 71] on radar point clouds has been found inadequate and generalises poorly. On the other side, recent mmWave radar scene flow estimation works [20, 21] generally focus on autonomous driving scenarios and rely on deep learning-based pipelines. However, these existing methods cannot be readily applied to our human sensing scenarios because the rigid-body assumption used for autonomous driving scenarios cannot stand in our cases where human subjects have non-rigid motion.

To cope with the above challenges, we propose *milliFlow*, a novel mmWave radar-based scene flow estimation for human motion sensing scenarios. Our contributions include:

- To the best of our knowledge, *milliFlow* is the first-of-its-kind work that aims to estimate mmWave radar-based scene flow for human motion sensing applications.
- We address the techniques challenges, e.g., sparsity, and lack of temporal cues, for scene flow estimation learning in our cases with a bespoke end-to-end learning network.
- We propose a cross-modal automatic pseudo scene flow labelling scheme specific for human motion sensing, avoiding labour-intensive manual labelling.
- We collect a large-scale human sensing dataset with 12 participants performing 8 different activities in three sites for evaluation, and perform a comprehensive evaluation of scene flow estimation accuracy as well as the performance on three downstream tasks.
- We open source our code and dataset to benefit the mmWave radar human sensing research communities.

2 SFCW MMWAVE RADAR PRELIMINARY

In contrast to the commonly used mmWave FMCW radars in previous studies [73–75], we employ the Vayyar radar [4] for our work, which is a stepped-frequency continuous-wave (SFCW) radar [70] bespoke designed for fine-grained human sensing. While both FMCW and SFCW radars can generate a point cloud from raw data for each frame, their underlying principles are slightly different. This section aims to provide a concise overview of the point cloud generation principles of SFCW radar to aid in comprehending the hardware components of the proposed system. In what follows we introduce the working principle of SFCW radars.

Range Estimation. Similar to FMCW radar, we can also detect range information with a single Tx-Rx pair. For a CW radar, the transmitting signal can be written as $s(t) = A\sin(2\pi f_0 t)$, and the corresponding receiving signal from the reflection on an object at range R would be $s_r(t) = A_r\sin(2\pi f_0 t - \phi)$, where ϕ is the phase difference of the transmitting and receiving signals, and can be written as $\phi = 2\pi f_0 \frac{2R}{c}$. As a result, we are able to estimate the range as $R = \frac{c}{4\pi f_0} \phi$. Note that ϕ can only be in range $[0, 2\pi]$. As a result, for CW radar that works on a single frequency, the maximum unambiguous range is very limited. For example, if $f_0 = 2\text{GHz}$, $R_{max} = 7.5\text{cm}$. For SFCW radar, we are able to get the phase difference at different frequencies, which provides much richer information for range estimation. For two consecutive frequencies f_1 and f_2 , the frequency difference $\Delta f = f_2 - f_1$, and the phase differences at each frequency step are $\phi_1 = \frac{4\pi R}{c} f_1$ and $\phi_2 = \frac{4\pi R}{c} f_2$. We have the following equation:

$$\Delta\phi = \phi_2 - \phi_1 = \frac{4\pi R}{c} (f_2 - f_1) = \frac{4\pi R}{c} \Delta f \quad (1)$$

and we get

$$R = \frac{c}{4\pi \Delta f} \Delta\phi \quad (2)$$

Also, we have $\Delta\phi \in [0, 2\pi]$, so the maximum unambiguous range is inversely proportional to Δf , which is the frequency step in SFCW radar. During each frame, the transmitter sequentially emits a series of waves of increasing frequency at equal intervals. The transmitted signal is reflected back at different surfaces in the scene and received by the receiving antenna. The ADC samples the change in amplitude and phase between the transmitted signal and the received signal and stores the values in IQ format. We can apply Fourier Transform to get the phase variation, with which we can further derive the range of the objects. This works as the 'range-FFT' for SFCW radar. The range resolution is inversely proportional to the bandwidth of the radar, written as $R_{res} = \frac{c}{2B}$, where $B = f_{max} - f_{min}$.

Angle-of-arrival Estimation. Angle-of-Arrival (AoA) estimation can be performed using a linear receiver array with equally-spaced elements, typically separated by a distance

of $1/2\lambda$, where the number of elements in the array, denoted as N , is greater than or equal to two. When a reflected signal is received at each element of the array, a phase difference arises due to the slight differences in signal travel distance, as determined by the angle of arrival, θ . This phase difference can be quantified using the formula $\Delta\phi = kds\sin(\theta)$, where k represents the wave number and d is the distance between consecutive elements. The angle of arrival can then be estimated by analyzing the phase difference using a Fourier Transform technique, commonly referred to as "Angle-FFT". Vayyar uses Multiple-Input Multiple-Output (MIMO) array, and for each frame, we are able to get a 2D virtual antenna matrix, from which we can estimate azimuth and elevation AoA simultaneously.

Point Cloud Generation. For each frame, the raw data is stored as a complex matrix of size $N_a * N_e * M$, where N_a and N_e are the numbers of Tx-Rx antenna pairs (i.e., virtual antennas) in azimuth and elevation directions, respectively, and M is the number of frequency steps. First, the clutter removal is applied to focus on dynamic objects. We then apply Range-FFT for Range estimation for each virtual antenna, and further perform 2D Angle-FFT to get the AoA information on both directions. Following the above processing, we are able to get a 3D heatmap for each frame. Strong peaks are then detected with methods like CFAR [53], and converted to 3D points, which is the input to our scene flow estimation.

3 TECHNICAL CHALLENGES

After understanding the working principles behind the SMFW mmWave radar, we now elaborate on the technical challenges of using it for human motion sensing.

Sparsity and Noise. Due to the bandwidth and hardware limitations, the heatmap used to detect targets has low resolution in both range and angular dimensions. Moreover, only outstanding peaks are selected from the heatmap as valid targets. As a result, the radar point cloud returned by related algorithms (e.g. CFAR [53]) is inevitably sparse with only an average of ~ 100 points correlated to human body. Some body parts even do not have their correlated radar points. More seriously, due to the multi-path effect of mmWave, there are a non-negligible number of ghost points in the radar point cloud that further poisons the original sparse radar data. Such sparse and noisy natures yield mmWave radar scene flow estimation non-trivial as the local geometric cues tend to be insufficient and low-quality. Concretely, it is hard to extract strong local features for each radar point with their scarce or absent neighbour points, which is further exacerbated by the non-negligible noisy points in radar point clouds, making the local features less robust.

Lack of Temporal Cues. Representing the radial velocity of each point, the radar Doppler velocity measurement

has great potential to benefit our radar scene flow estimation. Unluckily, the resolution of Doppler velocity measurement is limited by the hardware and is usually inadequate (e.g. >0.15 m/s) to identify the real motion status of objects, especially in human sensing scenarios, where the scale of movement is small. Furthermore, some radar products, for example, the Vayyar radar [4] used in this work, do not support the measurement of the Doppler velocity with only one excerpt of CW emitted per frame. The low resolution or absence of the Doppler velocity makes accurate scene flow estimation difficult. Particularly for those points that do not have associated points in the next frame, they cannot get any useful guidance from two worlds for scene flow estimation. Unfortunately, certain body parts (e.g. head, arm and leg) are often missing in radar point clouds, which means they do not have correlated radar points in the vicinity. Such inconsistent local capture together with the issue of Doppler velocity jointly pose another challenge to our method in the aspect of temporal information.

Scene Flow Annotation. In this work, as we rely on deep networks to learn accurate scene flow estimation, it is essential for us to have point-level scene flow labels that can be leveraged to supervise the network output. However, manually annotating point-wise scene flow is extremely expensive and suffers from the lack of real correspondence between real-world point clouds. Therefore, instead of labelling point by point from the ground, some recent works [20, 28, 31] adopt a top-down scheme that only annotates the bounding box of ambient objects and utilizes them to generate point-level pseudo scene flow ground truth. This object-based labelling scheme works well for autonomous driving scenarios as almost all road users (e.g. car, truck, motorcycle) can be seen as rigid bodies. However, despite the cost used for obtaining object annotations, the rigid-body assumption cannot hold in our human sensing applications where the motion of each human objective is non-rigid.

4 METHODOLOGY

We now introduce our proposed method to address the above technical challenges.

4.1 Overview

We formally formulate the scene flow estimation problem in Sec. 4.2. Sec. 4.3 details the design of the neural network that takes consecutive radar point clouds as the input and outputs the scene flow. Particularly, to address the sparsity and noise challenges, we propose to aggregate the global features to complement the vulnerable local features (c.f. Sec. 4.3.2). In the form of representation vectors, such global features can aggregate the features of all points and provide holistic information about a point cloud. Then, to compensate for the

absence of Doppler velocity and inconsistent local capture, we propagate the temporal information to the current frame using a GRU network [16] to update the global vectors of the flow embedding (c.f. Sec. 4.3.4). This strategy is intuitive as radar data is captured in sequence. Fig. 2 illustrates the architecture of our scene flow network. Last but not least, to efficiently label point-based scene flow for our training, we propose a cross-modal automatic scene flow labelling scheme (c.f. Sec. 4.4), specific to point clouds captured in human sensing scenarios. Our motivation is based on the observation that human body can be roughly segmented into multiple skeletons each of which can be seen as rigid bodies, such as the upper arm, neck and thigh bone. We then attribute the human dynamics to the rigid motion of these skeletons and further assume that the scene flow of points in the vicinity is induced by them. Given this assumption, we can first calculate the rigid transformation of skeletons and use them to annotate scene flow vectors for points attributed to them. The labelling pipeline can be seen in Fig. 3.

4.2 Problem Formulation

Here, we consider the problem of scene flow estimation for dynamic 3D point clouds collected by an SFCW mmWave radar sensor (c.f. Section 2) in human sensing scenarios. As a general problem setting, the input to point cloud-based scene flow estimation is two consecutive 3D point clouds $\mathcal{P} = \{p_i\}_{i=1}^N$ and $\mathcal{Q} = \{q_i\}_{i=1}^M$ captured by the same device and the output is a set of 3D vectors $\mathcal{F} = \{f_i\}_{i=1}^N$ that align each point p_i in \mathcal{P} to its associated position $p_i^a = p_i + f_i$ in the frame of \mathcal{Q} . Different from the task that finds real correspondences between two frames, scene flow only represents per-point 3D displacement for \mathcal{P} and the associate position p_i^a does not necessarily overlap with any points in \mathcal{Q} . Besides 3D coordinates information, each point may also have additional properties given mmWave radar point clouds as input, such as Doppler velocity or intensity value. Without losing generality, here we concatenate the per-point incident properties and 3D point coordinates into the 2D matrix and use $\mathcal{X} = \{x_i\}_{i=1}^N$, $\mathcal{Y} = \{y_i\}_{i=1}^M$ to denote the data from the source and target frame, respectively.

4.3 Scene Flow Network

Following the state-of-the-arts [20, 24, 35, 69], we rely on end-to-end trainable deep networks to learn scene flow estimation offline and apply the trained model to infer scene flow for upcoming radar point clouds online. Our scene flow network architecture can be seen in Fig. 2. In the following, we will first introduce five modules of our network in detail.

4.3.1 Local Feature Abstraction. In our network, we adopt the set abstraction layer proposed in PointNet++ [51] as the

basic learning layer to extract local point features. The working process of the local feature abstraction module can be found in Fig. 2. With two mmWave radar point clouds \mathcal{X} and \mathcal{Y} as input, we first encode their local features respectively using four parallel set abstraction (SA) layers [51]. These SA layers have different grouping radii and each of them extracts the local feature $l_{i,s}$ for each radar point at a specific scale s . Such multi-scale local feature abstraction is more insensitive to the non-uniform density of radar point clouds. We further use a shared-weighted MLP to map the local feature $l_{i,s}$ into a higher-level representation $k_{i,s} = \text{MLP}(l_{i,s}; \theta_s)$, where θ_s is the layer parameters for the scale s . For each point cloud, we concatenate the high-level local features from different scales and obtain the multi-scale local features $\mathcal{K}^{\mathcal{X}}, \mathcal{K}^{\mathcal{Y}}$ for two input point clouds. Besides, we also utilize a context feature extractor to encode the context features $\mathcal{K}_c^{\mathcal{X}}$ of point cloud \mathcal{X} . Note that this context extractor does not share weights with the local feature encoder but they have the same structure and hyperparameters. The extracted context feature is utilized in Sec. 4.3.3 to provide the context information to the flow embedding.

4.3.2 Global Feature Aggregation. As the first step, the local feature vector of each radar point is mapped into a scalar $w_i = \text{MLP}(k_i; \theta_a)$, where θ_a is the learnable parameters for the attention mapping. To ensure numerical stability, we normalize all attention weights to sum to 1. Then, the global feature vector g can be obtained by aggregating the local features of all points with a weighted sum operation, which is written as:

$$g = \sum_{i=1}^N w_i \cdot k_i \quad (3)$$

Compared with the max-pooling operation that discards almost all information in local features, this attention-based aggregation can learn to dynamically adjust the weights and combine the information from all points. Finally, we concatenate this global vector to the local feature of each point and obtain the local-global representations $\mathcal{Z}^{\mathcal{X}}, \mathcal{Z}^{\mathcal{Y}}$ for radar frames \mathcal{X} and \mathcal{Y} . Similar to local feature abstraction, we also extract the global feature for the context feature $\mathcal{L}_c^{\mathcal{X}}$ using another MLP and denotes its output as $\mathcal{Z}_c^{\mathcal{X}}$.

4.3.3 Flow Embedding Generation. To encode points motion between two radar frames, we leverage the point cloud cost volume (CV) layer in [71] to correlate features. Given the local-global features of two radar point clouds, i.e., $\mathcal{Z}^{\mathcal{X}}, \mathcal{Z}^{\mathcal{Y}}$, we use the CV layer [71] to compute the correlation between them, as seen in Fig. 2. By aggregating the spatial relationship and feature similarities between two frames, the point motions are encoded into the cost volumes, denoted as $\mathcal{O} = \{o_i\}_{i=1}^N$. Thanks to the global feature aggregation, the holistic frame information can also be correlated, which

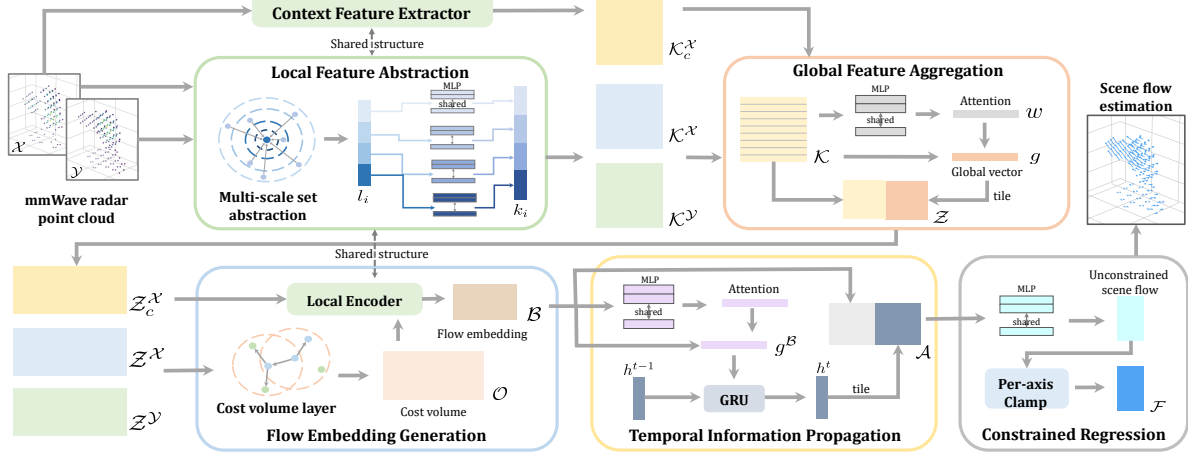


Figure 2: Scene flow network architecture.

yields more robust and stable costs. The CV layer enables us to decode the scene flow vector for each point as it contains the motion information between two frames. To further mix it with the context, we then stack the cost volumes \mathcal{O} , context features \mathcal{L}_C^X and pass the features into another local encoder to obtain the flow embedding $\mathcal{B} = \{b_i\}_{i=1}^N$.

4.3.4 Temporal Information Propagation. Directly propagating 2-dimension flow embedding from previous frames suffers from a) high computation overload, b) the change in the number of points between frames. To overcome these issues, we propose to temporally update its global vector instead of the flow embedding itself, as shown in Fig. 2. More specifically, we first follow the same process as in global feature abstraction to generate the global vector g^B of the flow embedding \mathcal{B} . Then we apply a GRU network [16] to update it as hidden states temporally and obtain the final global representation $h^t = \text{GRU}(h^{t-1}, g^B; \theta_g)$, where h^{t-1} is the global representation from the last frame and θ_g is the GRU network parameters. Lastly, we concatenate this updated global representation to each point in the flow embedding and denote the final features as $\mathcal{A} = \{a_i\}_{i=1}^N$.

4.3.5 Constrained Scene Flow Regression. Given the final features \mathcal{A} produced above, we can use an MLP-based flow regressor to decode per-point scene flow $\mathcal{F} = \{f_i\}_{i=1}^N$. However, estimating unconstrained scene flow may lead to non-viable results, e.g., the magnitude of the flow vector exceeds the normal scale of human body movement. To constrain our predictions, we propose to clamp the estimated scene flow before returning it. We set a fixed threshold ϵ and constrain the scene flow on each axis to be within the range of $[-\epsilon, \epsilon]$.

4.4 Automatic Scene Flow Labelling

To cope with the human sensing scenarios where non-rigid human motion dominates, we propose a new cross-modal

automatic scene flow labelling scheme, as shown in Fig. 3. With the help of co-located RGB-D camera, we first label 3D human skeletons and then generate noisy pseudo scene flow labels based on the skeleton-based rigid-motion assumption.

Human Skeleton Annotation. In human sensing applications, the human skeleton is usually characterised by the 3D position of its two endpoints, aka. keypoints. To quickly and conveniently annotate such keypoints, we refer to the RGB-D images recorded by co-located depth camera in this work. Specifically, we first utilize an open-source pose estimation library (e.g. OpenPose [13]) to label 2D keypoints on RGB images and then uplift each 2D keypoint to 3D using its corresponding depth value. Then the human skeleton labels can be obtained using intrinsically connected 3D keypoints.

Pseudo Label Generation. Given the 3D skeletons automatically annotated above, we can generate pseudo scene flow labels $\tilde{\mathcal{F}} = \{\tilde{f}_i \in \mathbb{R}^3\}_{i=1}^N$ for radar point clouds. For two consecutive point clouds \mathcal{P} and \mathcal{Q} , we first compute the inter-frame transformation matrix for all human skeletons in the source frame. Then we assign each source radar point p_i to its closest skeleton. In the final, we derive the pseudo scene flow labels for each selected radar point as $\tilde{f}_i = (T_j \circ p_i) - p_i$, where $T_j \in \mathbb{R}^{3 \times 3}$ is the transformation matrix for the skeleton that point p_i is assigned to. \circ is the action that operates homogeneous transformation for 3D points.

Keypoint-Based Label Filtering. Due to the errors induced by the keypoint estimator, our generated pseudo scene flow labels are prone to have much noise. To mitigate the impact of these errors, we propose to filter our labels based on the confidence scores and the displacement of estimated keypoints. First, we retrieve the confidence scores from the 2D keypoints estimator and filter out those keypoints whose

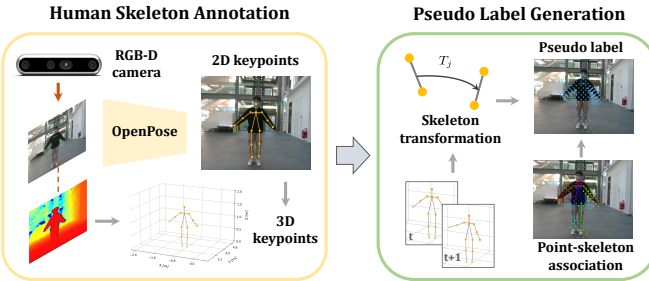


Figure 3: Automatic scene flow labelling pipeline.

confidence is lower than 0.5. Then, we calculate the 3D displacement for the left keypoints between two frames and further discard keypoints whose displacement is bigger than 0.5m. After the above two-stage filtering, we obtain a set of valid keypoints for each frame. Skeletons whose two keypoints are both valid are identified as valid and we generate a mask $\mathcal{M} = \{m_i \in \{0, 1\}\}_{i=1}^N$ to discard the pseudo scene flow labels associated with the invalid skeletons, where valid labels are marked as 1. This mask can be used to mitigate the impact of noises in our loss function (c.f. Sec. 4.5).

4.5 Loss Function

We use the generated pseudo scene flow label $\tilde{\mathcal{F}}$ (c.f. Sec. 4.4) to supervise our scene flow network output \mathcal{F} . Specifically, we apply the valid mask $\mathcal{M} = \{m_i\}_{i=1}^N$ to discard the impact of the identified noisy labels when calculating the loss values. However, in our initial experiments, we find that network easily gets stuck into the local minima where almost all estimated scene flow vectors are close to a small fixed value. We credit this to the fact that most points have small-scale movements, which may dominate our network training and lead it to stay in a *comfort zone* (i.e., the local minima) by producing small and identical results for various inputs.

To help our network to escape from the local minima, we propose to weigh points with large-scale movements more when computing the training loss. Specifically, we separately calculate the average loss for points whose scene flow label is larger than a threshold ζ and combine it with the average loss of other points. Our loss function can be written as:

$$\mathcal{L} = \alpha_l \mathcal{L}_{large} + \alpha_s \mathcal{L}_{small} \quad (4)$$

Here, α_l and α_s are the hyperparameters to balance the impact of large- and small-scale movements. By giving points with large-scale movement more weight in our loss, we can dilute the domination of the majority small-scale points, especially those static points, and thus avoid the local minima.

5 IMPLEMENTATION

5.1 Dataset Collection

5.1.1 Sensing Platform. As exhibited in Fig. 4 (a), we use a commercial Vayyar vTrigB imaging mmWave radar [4] and a

RealSense D455 depth camera [1] to capture mmWave radar point clouds and RGB-D images respectively. The mmWave radar device is portable with a size of 10.4 cm \times 8.5cm and a weight of 110g in total, emitting SFCW to the surroundings to receive the RF signals. The internal data processing pipeline of this device follows the steps we illustrate in Sec. 2. The final output is a set of 3D points with per-point intensity values. For the depth camera, the RGB-D image size is set as 640 \times 480 and its depth measurement range is from 0.6m to 6m. Both sensors are fixed on a spoken collection board to ensure their relative position is unchanged after the initial calibration. We further mount this board on a tripod with a height of about 1.3m, as seen in Fig. 4 (a). During collection, we alternately query the data frame from two sensors and stored them in a PC, resulting in the synchronized mmWave radar point clouds and RGB-D images. The average frame rate over all collected data is $\sim 13.2\text{Hz}$.

5.1.2 Collection Subject. 12 participants of various genders, ages, heights and weights are recruited for data collection in this work². To evaluate the effectiveness of methods in different scenes, we choose three sites, as shown in Fig. 4 (c), including the hallway, parking lot and square as our human sensing experiment scenes. For each scene, each participant is asked to perform 5 'in-set' activities, namely bicep curl, arm swing, bowing, leg swing, and arm & leg swing, as seen in Fig. 4 (d), each of which lasts for about 20s. The collection platform is placed about 2.5 – 3.5m away from the subject. Every subject is asked to wear a face mask to protect their identities from being recognised. After data collection, we manually crop each sequence to 200 frames for uniform activity distribution. As a result, the whole main dataset consists of $12 \times 3 \times 5 \times 200 = 36\text{k}$ frames in total. To test the generalization ability to unseen subjects, we divide the dataset into three parts by subject. 6 people are used for training, while 2 people are used as the validation set and the remaining 4 people are used for testing. Besides the main dataset, we also collect an 'out-of-set' testing set by letting all people perform three 'out-of-set' activities, including squatting, sitting and head bobbing as shown in Fig. 4 (d), in the hallway site to evaluate the generalization to unseen activities. This extra testing set is composed of $12 \times 3 \times 200 = 7.2\text{k}$ frames.

5.2 Evaluation Setup

5.2.1 Data Preprocessing. Given sequences of mmWave radar point clouds, we first filter them by range to discard points outside our region of interest. The side, forward and height range in the radar coordinate frame is set as $[(−3, 3), (0.5, 5),$

²The study has received the ethical approval from XXX (no name for blind review), and participant consent forms were signed before the collection.

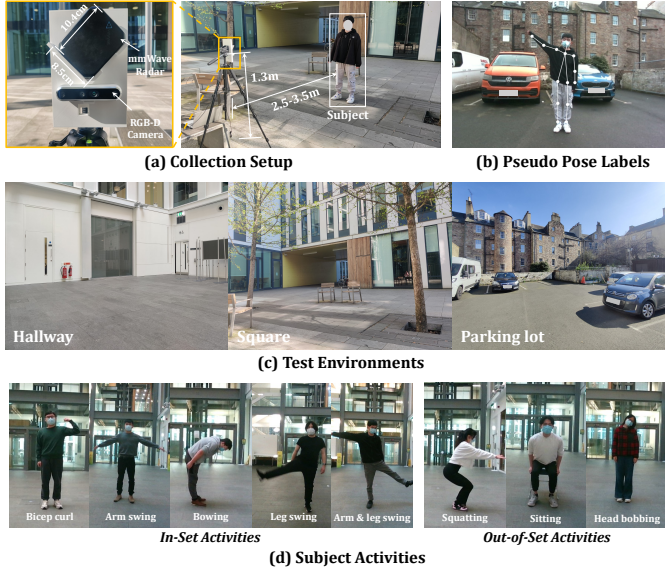


Figure 4: Collection setup, test environment, subject activities and an example of pseudo pose labels.

(-1.5, 1.5)] meters respectively. We then filter points by intensity to omit the background points. The intensity threshold is empirically set as 0.5. For all training and validation frames, we randomly sample 128 points from each radar point cloud to facilitate fast mini-batch-based training. We keep the number of points unchanged in all testing frames to make sure that the scene flow estimation for each point can be examined. In the end, we generate scene flow samples by combining pair-wise frames. Each 200-frame sequence can produce 199 samples, each of which consists of two consecutive mmWave radar point clouds and their corresponding RGB-D images.

5.2.2 Labelling. We use our proposed automatic labelling scheme (c.f. Sec. 4.4) to annotate scene flow for training and validation samples. Specifically, we keep 14 keypoints from the off-the-shelf pose estimator to represent the subject pose following [52, 73], which results in 13 connections between intrinsically connected keypoints as seen in Fig. 4 (b). We then omit invalid skeletons with our two-stage label filtering and annotate the pseudo scene flow labels for points belonging to the valid ones. For our testing samples, we follow the same labelling pipeline but annotate all points. To make the testing labels accurate enough, we add manual inspection and correction for the estimated 2D keypoints.

For the human action recognition (HAR) task, we manually label the ground truth of human activity for each sequence during recording. To annotate human parsing (HP) labels, we utilize the point-skeleton affiliation information generated during scene flow labelling and label each point with the body part it belongs to. Specifically, as the skeleton labels generated during training are noisy, we also introduce the

Method	EPE3D (m) ↓			Acc3D ↑	
	All	Moving	Static	Strict	Relax
FlowNet3D [43]	0.293	0.290	0.259	0.016	0.095
PPWC-Net [71]	0.171	0.181	0.128	0.138	0.179
Graph Prior [49]	0.315	0.322	0.283	0.007	0.011
FLOT [50]	0.299	0.307	0.265	0.015	0.094
FlowStep3D [35]	0.243	0.251	0.216	0.062	0.109
PV-RAFT [69]	0.161	0.170	0.107	0.179	0.292
RaFlow [21]	0.107	0.115	0.094	0.271	0.427
Bi-PFNet [15]	0.159	0.168	0.111	0.153	0.264
milliFlow (ours)	0.046	0.051	0.009	0.406	0.703

Table 1: Comparison of scene flow estimation results.

valid mask \mathcal{M} (c.f. Section 4.4) to our HP task to discard invalid points for training. The testing labels for the human body part tracking (HBPT) task are ready to use as we already obtain the 3D keypoints during scene flow labelling.

5.2.3 Evaluation Metric. We use the following evaluation metrics to quantify the performance on scene flow estimation and downstream human sensing tasks.

- **EPE3D (m).** It computes the average 3D endpoint error $\|f_i - f_{gt}\|_2$ over all points in a frame. Following [9, 21], we also report the errors separately for the *moving* and *static* points. Points with a ground truth flow vector larger than 0.01m are labelled as *moving*.
- **Acc3D.** It measures the ratio of points in one frame that meets the relax/strict accuracy requirements, i.e., either $EPE3D < 0.025/0.05$ m or relative error <5%/10%.
- **Overall accuracy (oA) (%).** It measures the proportion of examples for which the predicted label matches the single target label, i.e., $\frac{TP+TN}{TP+FP+TN+FN}$. In our experiments, we use it to formulate HAR and HP problems as per-sequence and per-point classification problems.
- **Mean Intersection over Union (mIoU) (%).** For a single body part class, its IoU is defined as $\frac{TP}{TP+FP+FN}$, measuring the overlap between the predicted subset of points and the ground truth one divided by their union. The mean IoU (mIoU) score is calculated by averaging scores on all body part classes. In our evaluation, we use this metric for our HP tasks to show the paring results.
- **Mean Joint Localization Error (mJE) (m).** This metric is used for our HBPT task. We define it as the mean 3D Euclidean distance between the positions of endpoints of the tracked body parts and their ground truth positions.

5.2.4 Network and Training Details. For scene flow network, the grouping radii for four SA layers used for local or context feature extraction are [0.05, 0.1, 0.2, 0.4] meters. The numbers of local samples for them are set as [4, 8, 16, 32] and the dimension of the MLP used in and after each SA layer is [32, 32, 64], [64, 64, 64] respectively. In all global feature aggregation, the MLP used for attention mapping is two-layer

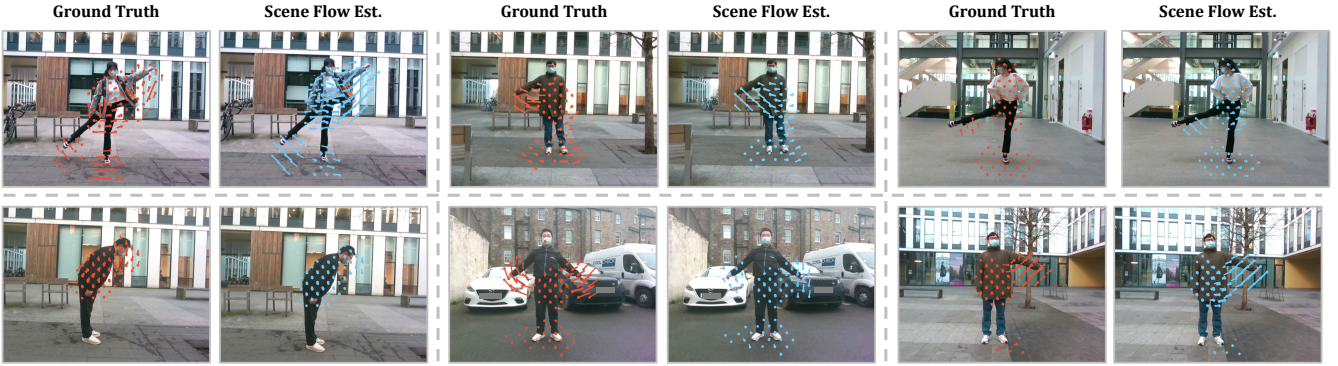


Figure 5: Qualitative scene flow estimation results. To make our results more readable, we project radar points and scene flow vectors onto the image plane for visualization. We use red for the ground truth while blue for ours.

with a hidden dimension of 128. In the CV layer, the number of neighbours for patch-to-patch aggregation is set as 8 and each MLP used to learn aggregation weights has three layers with hidden dimensions of [8, 8]. The local encoder used to generate flow embedding has the hyperparameters as the former one except for its MLP that has the dimension of [512, 256, 64] in each SA layer. The dimension of the flow regressor MLP is [256, 128, 64, 3] and the threshold ϵ to constrain the output is set as 0.1m.

To implement our temporal propagation (c.f. Sec. 4.3.4), we divide the long sequence of scene flow samples into many mini-clips with a length of 5 frames and train using mini-batches of them after shuffling. During inference, we re-initialize the hidden state of the GRU to zero vectors after 5 frames to fit the training pattern. The threshold ζ used for our loss function (c.f. Eq. 4.5) is fixed as 0.1m for all experiments while the weight hyperparameters α_l and α_s is set as 2 and 1. For all training in our experiments, we consistently use the Adam optimizer with an initial learning rate of 1e-3, which decays by 0.9 after each epoch. The performance on the validation set is used to determine when to stop the training process and to select the best model for each training experiment. More details on how to implement our downstream tasks can be found below in Sec. 7.

6 SCENE FLOW EVALUATION

6.1 Overall Performance

6.1.1 Compared to the state of the arts. We first compare our network with state-of-the-art methods of point-based scene flow estimation. Our baselines include 7 deep learning-based methods [15, 21, 35, 43, 50, 69, 71] whose networks are also supervised with pseudo scene flow labels, and one non-learning-based method Graph Prior [49] that solves scene flow via online optimization. The evaluation results on our testing set can be seen in Table 1. The scene flow network of milliFlow achieves a cm-level average EPE3D (i.e., 4.6cm)

and a high relax Acc3D of 70.3%, ranking 1st on all metrics with a large margin compared to the baselines. This satisfactory performance proves the efficacy of our method to address the challenges existing in our scene flow task. Note that our network is trained with pseudo labels automatically generated using RGB-D images (c.f. Sec 4.4), which does not demand any manual annotation efforts.

6.1.2 Qualitative results. Some examples of our scene flow outputs are demonstrated in Fig. 5. It can be seen that our method can produce reliable scene flow estimation for various activities performed by different subjects in three test environments. Despite the sparsity and noise of radar point clouds, our network can still effectively learn representative features thanks to our global feature aggregation (c.f. Sec. 4.3.2) and robustly regress scene flow vectors. As exhibited in our examples, some body parts are missing in radar point clouds, which impedes the scene flow inference process. We compensate for the temporal information shortage by utilizing the historical information to benefit the current scene flow estimation (c.f. Sec. 4.3.4), which yields sound testing performance across frames.

6.1.3 Runtime efficiency. We test the runtime efficiency of our scene flow network on a single NVIDIA RTX 3090 GPU. Given sequential testing radar point clouds, we feed them one by one into our trained model for inference. As a result, our model has real-time performance with one inference step in 74ms (~ 13.5 Hz). Moreover, the maximum allocated GPU memory is only 134 MB during inference. Such a low GPU memory consumption facilitates the parallel operation of scene flow and downstream networks.

6.2 Ablation Study

To validate the effectiveness of some key components in our scene flow network, we disable them one by one and investigate the impact on the results. Specifically, four components

	Method	EPE3D (m) ↓			Acc3D ↑	
		All	Moving	Static	Strict	Relax
(a)	Full version	0.046	0.051	0.009	0.406	0.703
(b)	(a) w/o TP	0.053	0.062	0.018	0.382	0.676
(c)	(b) w/o GA	0.061	0.068	0.025	0.361	0.628
(d)	(c) w/o CF	0.071	0.077	0.028	0.315	0.536
(e)	(d) w/o CR	0.083	0.090	0.034	0.286	0.490

Table 2: Breakdown results of our scene flow network.

are ablated from our network, including temporal propagation (TP), global aggregation (GA), context feature (CF) and constrained regression (CR). The ablation experiments results are exhibited in Table 2. Overall, the full version of our network (row (a)) yields the best results and each component helps to elevate the performance on each metric (from row (e) to (a)). First, our temporal propagation can effectively harness the information from previous frames to help scene flow estimation (c.f. Sec. 4.3.4), yielding a relatively 13.2% lower EPE3D and a 6.3% increase on strict Acc3D (comparing row (a) and (b)). Moreover, by leveraging our attention-based global feature aggregation (c.f. Sec. 4.3.2), the vulnerable local features can be largely augmented with holistic information, which brings another remarkable improvement over each metric (e.g. 13.1% on EPE3D). Besides, incorporating the context features into our flow embedding can help to preserve the context from the source frame after feature correlation (c.f. Sec. 4.3.3). This can be an auxiliary feature for the scene flow decoding. Although simple, this strategy, to our surprise, gives a non-trivial contribution to our performance with a decrease of 0.01m on overall EPE3D. Lastly, the biggest improvement (i.e., a 0.012m decrease on EPE3D) is brought by our constrained regression, in which the scene flow component on each axis is clamped by a fixed threshold (e.g. 0.1m). This is reasonable as non-viable results, for example, a scene flow vector with a length of 0.5m, can seriously degrade our results after averaging over all points.

6.3 Sensitivity Analysis

Impact of global aggregation mechanism. Besides the attention-based mechanism, another two typical operations, i.e., max-pooling and average-pooling, are tested into our network for global feature aggregation (c.f. Sec. 4.3.2). The comparison results are shown in Table 3. From the table, the attention-based mechanism yields the best performance as it can learn to dynamically adjust the weights according to per-point local features. The average-pooling performs better than the max-pooling. We credit this to the ability of the average-pooling to retain the mean feature across all points, which is more robust to outliers.

Impact of test environments. In Table 4, we report the results of our trained model on each scene individually. As we

Mechanism	EPE3D (m) ↓			Acc3D ↑	
	All	Moving	Static	Strict	Relax
Attention-based	0.046	0.051	0.009	0.406	0.703
Max-pooling	0.050	0.059	0.011	0.394	0.679
Average-pooling	0.047	0.055	0.009	0.399	0.698

Table 3: Comparison of global aggregation mechanisms.

Scene	EPE3D (m) ↓			Acc3D ↑	
	All	Moving	Static	Strict	Relax
Hallway	0.040	0.046	0.007	0.464	0.746
Square	0.042	0.049	0.009	0.435	0.722
Parking lot	0.051	0.058	0.011	0.374	0.671

Table 4: Results for different test environments.

can see, our model shows the best performance for the indoor scene (i.e., hallway) while performing worst in the parking lot scene. We credit the difference in performance between test environments to two factors. First, the background clutter in outdoor scenes, especially the parking lot (c.f. Fig. 4), is more complicated, which results in severer multi-path reflection during measurement. This decreases the SNR in radar data and further degrades the fidelity of generated radar point clouds. Second, our pseudo label generation (c.f. Sec. 4.4) is affected by the changeable outdoor illumination conditions. Not only does the 2D keypoint estimation on RGB images become more challenging, but also the depth measurements can be interfered with by the strong sunlight. Consequently, the quality of skeleton estimation in outdoor scenes is lower and the training is not as effective as in the indoor scene.

Impact of training subjects number. In the above experiments, the data from 6 subjects are used for training (c.f. Sec. 5.1.2). Here we utilize 2/3/4/5 people out of the training set respectively for training to analyze the impact of the number of training subjects. As seen in Figure 6, the performance of our network increases in all metrics as more subjects are added for training. This proves that there is still room to improve our performance when more training data is available. We can also observe that, even with only 3 training subjects (9k data frames), our network can still generalize well to the testing set with an overall EPE3D of 0.066m and a relax Acc3D of 0.56. This result further demonstrates the feasibility of our automatic scene flow labelling scheme (c.f. Sec. 4.4) to generate reliable pseudo labels.

6.4 Generalization to New Activities

In the above experiments, we evaluate our method on the testing set whose subjects are unseen during training. The results demonstrate the generalization ability of our trained model to new users that perform the same 'in-set' activities. To further test its generalization to new activities, here we evaluate our trained model on the 'out-of-set' testing

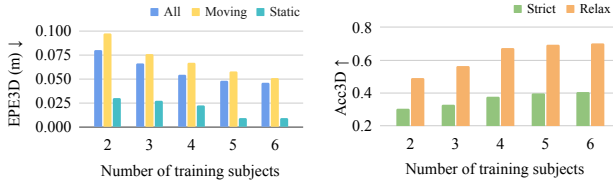


Figure 6: Impact of the number of training subjects.

Activity	EPE3D (m) ↓			Acc3D ↑	
	All	Moving	Static	Strict	Relax
Sitting	0.034	0.038	0.004	0.498	0.771
Squatting	0.040	0.047	0.009	0.416	0.688
Head bobbing	0.027	0.031	0.006	0.664	0.859
Average	0.034	0.039	0.006	0.526	0.773

Table 5: Generalization of our model to new activities.

set (c.f. Sec. 5.1.2) in which three performed activities are not included in the training set. We can see from Table 5 that, our trained model can still keep an equally good performance, compared to the results in hallway shown in Table 4, when encountering unseen activities. This demonstrates the ability of our model to cope with new activities in human sensing. As we investigate further we can observe that, on the head bobbing activity, our network achieves the best results across all metrics, achieving a high relax Acc3D of 0.859. We attribute this to the fact that most skeletons are static (except for the neck) when doing this activity (c.f. Fig. 4 (d)), and even for the only moving skeleton, the movement scale is still small. Therefore, estimating the scene flow of points belonging to them is much easier. Similarly, because all skeletons are moving during squatting (c.f. Fig. 4 (d)), it is more challenging for our model to infer scene flow on point clouds captured in this activity. We believe that our trained model can also generalize to other daily human activities.

7 DOWNSTREAM TASK EVALUATION

As a low-level signal in understanding motions, scene flow can directly enhance low-quality radar point clouds with full per-point displacement information between two frames. Moreover, the latent spatial-temporal representations can be implicitly learned by guiding the network to estimate scene flow, which can be used to support other tasks. Therefore, we envision that learning scene flow estimation can benefit a wide range of higher-level downstream tasks in mmWave-based human sensing. To demonstrate the benefit, here we consider three representative downstream tasks, including HAR, HP and HBPT for evaluation.

7.1 HAR Evaluation

7.1.1 HAR Network. HAR plays a significant role in a wide range of applications, such as elderly healthcare monitoring [58], smart home [11] and behaviour surveillance [33]. The goal of HAR is to identify the specific type of action of a person given a sequence of sensor data. As our focus is to validate the functionality of scene flow to benefit related tasks, here we only design one simple base network for HAR. Given a sequence of T radar point clouds together with their point-level features as input, we follow the process in local feature abstraction (c.f. Sec. 4.3.1) and global feature aggregation (c.f. Sec. 4.3.2) to extract the local-global representations for each point cloud. Then we use another local encoder to extract higher-level features and aggregate the global feature vector again for each frame. We utilize the LSTM network [27] to track the temporal relationship across T global vectors and then send the updated hidden state into a final MLP to regress the classification scores $S^a = \{s_i^a\}_{i=1}^K$ for K classes. The HAR network can be supervised with a simple cross-entropy loss that measures the difference between S^a and a one-hot ground truth activity label.

7.1.2 Scene Flow Application to HAR. We propose two strategies to harness the scene flow network as a plug-and-play module to the downstream network. We believe both of them can effectively improve downstream performance.

Point cloud decoration. The first way is to directly take the estimated scene flow as point-level raw features and decorate each radar point with them. Such additional scene flow features can explicitly provide the full motion information of radar point clouds. We adopt a two-stage training manner to implement this strategy, which first end-to-end trains the scene flow network and then freezes it to provide raw scene flow features to the downstream network training.

Latent feature recycling. Another way is to leverage the latent representations (c.f. Sec. 4.3.4) encoded by scene flow networks to enhance the low-quality radar point clouds. By guiding the network to estimate accurate scene flow, the learned representation can provide high-level spatial-temporal information to downstream networks in a specific aspect. We follow a joint learning fashion to implement this strategy that takes the final features from the scene flow network as the input features to the downstream network and trains these two networks *jointly* with a combination of the scene flow and downstream loss functions.

7.1.3 Performance on HAR. We evaluate our proposed two strategies for scene flow application to HAR task on our "in-set" testing set. The length of each input sequence T for HAR is set as 20 while the number of activity classes K is 5. The evaluation results are shown in Table 6. As we can

Method	HAR		HP		
	oA (%)	Gain (%)	mIoU (%)	oA (%)	Gain (%)
raw network	47.32	-	49.09	65.75	-
w. strategy 1	57.88	+10.56	52.72	69.27	+3.63 (+3.52)
w. strategy 2	57.78	+10.46	51.04	68.21	+1.95 (+2.46)

Table 6: Evaluation on the HAR and HP task.

see, both two proposed strategies can enhance the performance on HAR. Either point cloud decoration (i.e., strategy 1) or latent feature recycling (i.e., strategy 2) yields a remarkable improvement (>10%) in accuracy, demonstrating their usefulness in helping distinguish between different human actions. We also show the breakdown results (with strategy 1) on HAR as the confusion matrix in Fig. 7. As we can see, by decorating radar points with estimated scene flow, our HAR network achieves a high accuracy value on the bowing activity. However, the accuracy values on other activities are not as satisfactory as on bowing. For example, 42% leg swing samples are wrongly predicted as the arm & leg swing activity. This is due to the high similarity between these two activities and in some cases the arms also move with the leg swing, confusing the HAR network.

7.2 HP Evaluation

7.2.1 HP Network. HP aims to parse human semantic body segments (head, arms, torso, etc.) from sensor data. With radar point clouds as input, our objective of HP is to identify the body parts that correspond to each point. To evaluate the effectiveness of scene flow on this task, we also design a simple base network for this downstream task. Similar to HAR, HP network also takes sequential radar point clouds as input and utilizes local encoders as well as global aggregation to obtain the latent representation and a global feature vector for each frame. Differently, the human parsing task needs to estimate per-point classification scores for every point rather than the whole sequence. Therefore, after applying the temporal information propagation as in Sec. 4.3.4, we use the point-level final features to regress the parsing scores $S^p = \{s_i^p\}_{i=1}^V$ for each point. Here V denotes the number of human body segments. Our HP network is also supervised using a cross-entropy loss with per-point parsing labels. Specifically, we average the loss values over all classes to balance their impact to training. Please see Sec. 5.2.2 for our labelling and denoising process for the HP tasks.

7.2.2 Performance on HP. We use the same two strategies proposed in Sec. 7.1.2 to apply scene flow to the HP task on the "in-set" testing set. The number of body segments for parsing V is 6, including two arms, two legs, head and torso. Leveraging scene flow in two strategies also contributes to better performance on the HP task. Specifically, we observe that directly decorating points with scene flow (i.e., strategy

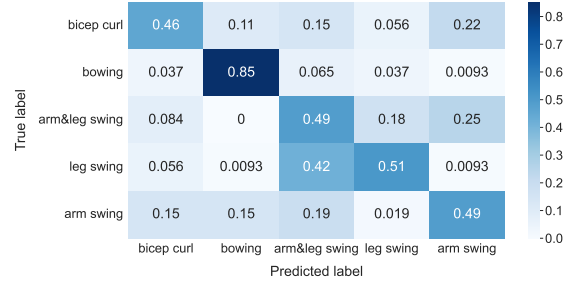


Figure 7: Confusion matrix of HAR.

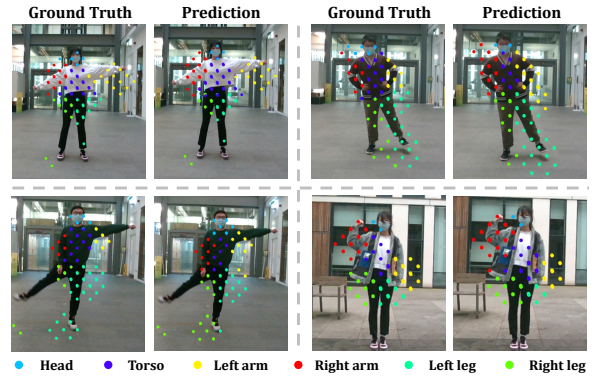


Figure 8: Human parsing results visualization.

1) leads to a larger gain than the implicit latent feature recycling (i.e., strategy 2). This is reasonable as our trained scene flow network can provide explicit and reliable per-point full-motion information to downstream tasks, while the learned latent features are implicit and demand further encoding for functioning. Moreover, unlike the two-stage training strategy that only considers one task per time, the scene flow regression and downstream tasks need to be balanced in our joint training fashion, sacrificing their task-specific performance more or less. However, in strategy 2, we only need to run the training once, which is simple to be implemented in real-world applications. Some examples of our HP results (with strategy 1) are exhibited in Fig. 8. It can be seen that our method can accurately parse radar point clouds into different body parts, close to the ground truth results.

7.3 HBPT Evaluation

7.3.1 Scene flow Application to HBPT. Given the initial position of a part of the human body, our HBPT task aims to track its movement in subsequent frames. Based on our assumption in Sec. 4.4, the human body part can be represented by a human skeleton that is characterized by its two endpoints. As a result, our goal becomes to estimate the transformation matrix of this rigid skeleton given the per-point scene flow estimation, which can be seen as the reverse process of our scene flow labelling. Given point-level scene flow estimation,

Activity	Tracking length - mJE (m) ↓			
	1	2	3	4
Arm swing	0.028	0.076	0.097	0.124
Leg swing	0.016	0.071	0.105	0.13
Arm & leg swing	0.030	0.108	0.146	0.178
Average	0.025	0.085	0.116	0.144

Table 7: Scene flow-based HBPT evaluation results.

we first group N_t radar points that can be assigned to the skeleton needed to be tracked. Then we generate natural correspondences $\{p_i, p_i + f_i\}_{i=1}^{N_t}$ using their scene flow and apply the classical Kabsch algorithm [32] to solve the rigid skeleton transformation based on them. The new positions of two endpoints can be obtained by applying the transformation to their last positions. By repeating the above steps, we can track a human body part in as many subsequent frames. Note that our method only demands a pre-trained scene flow network and does not need any extra training effort.

7.3.2 Performance on HBPT. We select the sequences of arm swing, leg swing and arm & leg swing activities in the testing set for HBPT evaluation. Specifically, we take the two arms, two legs and both of them, in these three activities respectively as our HBPT targets that are tracked independently across frames. For implementation, we divide the long sequences into short clips with a length of 5 frames and track the body parts within each clip. After initializing the ground truth positions in the first frame, we aim to track each skeleton for the next four frames. The HBPT results at different tracking lengths on three activities are reported in Fig. 7. With accurate scene flow estimation, we can effectively track multiple body parts together for different activities. For one-frame tracking, our method achieves an average mJE of <3cm on three activities, demonstrating the capability of scene flow to enable the HBPT task. However, the errors become larger as the tracking length increases, which indicates the happening of the tracking drift. This is inevitable for our method as more radar points associated with other skeletons will be wrongly induced for transformation calculation when the tracking continues. We also observe that the performance on arm & leg swing activity is worse than another two activities. This is reasonable as we need to track twice the skeletons in this activity as others, where more skeletons may interfere with each other.

8 RELATED WORK

mmWave Radar-based Human Sensing. The feasibility and versatility of mmWave radar have been extensively demonstrated in various human sensing applications, including vital sign monitoring [7, 44, 67], fall detection [30, 61], human tracking and identification [17, 75, 76], hand gesture

recognition [26, 40, 41], activity recognition [6, 56, 66] and pose estimation, reconstruction [36, 72, 73]. Compared with these applications, our work is unique in that we aim to estimate point-level scene flow vectors instead of providing a holistic output for the whole point cloud. In this way, we can either explicitly augment each radar target with scene flow vectors or implicitly learn robust latent features, which can further benefit a wide range of downstream sensing tasks, such as HAR, HP and HBPT (c.f. Sec. 7).

Scene Flow Estimation on Point Clouds. Recent scene flow works are mostly towards autonomous driving applications and attempt to estimate scene flow on LiDAR point clouds captured from autonomous vehicles. To this goal, different approaches are proposed, including classical methods [19, 39, 49] and deep learning-based ones [9, 43, 69, 71]. Recently, with the advances in point cloud feature learning, deep learning-based methods become more prevalent. According to their learning paradigm, prior works in this thread can be divided into fully-supervised [10, 50, 63, 68, 69], self-supervised [9, 35, 38, 46, 71] and weakly-supervised [22, 24] learning approaches. Apart from the aforementioned works, our work aims to estimate scene flow for human sensing using mmWave radar. Moreover, our method does not demand any manual annotation efforts, instead, we automatically generate noisy pseudo scene flow labels from corresponding RGB-D images captured by the co-located camera.

Scene Flow Estimation with mmWave Radar. As far as we know, there are limited works that estimate scene flow using mmWave radar. A pioneering work [21] proposes a self-supervised learning pipeline for automotive radar scene flow estimation, where three specific loss functions and a two-stage network are bespoke designed for radar point clouds. To improve scene flow performance and enable more downstream applications, a later work [20] exploits cross-modal supervision from co-located sensors (e.g. IMU, LiDAR) on modern autonomous vehicles for radar scene flow learning. However, these methods cannot be transferred to human sensing scenarios due to two reasons. First, the radar used for human-centric applications is different from the automotive radar in many aspects, such as measurement properties and their resolution. More importantly, the human object is a non-rigid body, while in autonomous driving, scene dynamics are usually attributed to rigid body motion (e.g. cars and motorcycles) [19, 22, 24]. Such discrepancy in objective indicates different label and supervision generation schemes.

9 CONCLUSION

In this paper, we propose *milliFlow*, a novel deep learning framework that estimates point-wise scene flow information to complement 3D mmWave radar point cloud, specifically tailored for human motion sensing scenarios. To address the challenges posed by the instability and sparsity of mmWave

point clouds, our method utilizes multi-scale local features, which are enhanced with global features and temporal information. Additionally, we propose an automated labeling approach for network training to alleviate the need for costly manual labeling. Through extensive experiments conducted on our collected dataset, we demonstrate the superior performance of our proposed method, which is further validated through experiments on three downstream human sensing tasks. We believe that our proposed system can work as a perfect plug-in module in human motion sensing pipelines, offering rich motion features for downstream tasks and advancing the performance of mmWave radar-based human motion sensing systems to new heights.

REFERENCES

- [1] 2023. Intel® RealSense™ Depth Camera D455. <https://www.intelrealsense.com/depth-camera-d455/>
- [2] 2023. IWR6843ISK Evaluation board | TI.com. <https://www.ti.com/tool/IWR6843ISK>
- [3] 2023. rescueproject. <https://rescuerproject.eu/technology-tools/>
- [4] 2023. Vayyar Imaging - Home - Vayyar. <https://vayyar.com/>
- [5] 2023. wholehome-ai-sensor. <https://consumer.huawei.com/cn/wholehome/ai-sensor/>
- [6] Karan Ahuja, Yue Jiang, Mayank Goel, and Chris Harrison. 2021. Vid2Doppler: Synthesizing Doppler radar data from videos for training privacy-preserving activity recognition. In *Proceedings of the 2021 CHI Conference on Human Factors in Computing Systems*. 1–10.
- [7] Mostafa Alizadeh, George Shaker, João Carlos Martins De Almeida, Plinio Pelegrini Morita, and Safeddin Safavi-Naeini. 2019. Remote monitoring of human vital signs using mm-wave FMCW radar. *IEEE Access* 7 (2019), 54958–54968.
- [8] Davide Baltieri, Roberto Vezzani, and Rita Cucchiara. 2011. 3dpes: 3d people dataset for surveillance and forensics. In *Proceedings of the 2011 joint ACM workshop on Human gesture and behavior understanding*. 59–64.
- [9] Stefan Andreas Baur, David Josef Emmerichs, Frank Moosmann, Peter Pinggera, Björn Ommer, and Andreas Geiger. 2021. SLIM: Self-Supervised LiDAR Scene Flow and Motion Segmentation. In *Proceedings of the IEEE/CVF Computer Vision and Pattern Recognition Conference*. 13126–13136.
- [10] Aseem Behl, Despoina Paschalidou, Simon Donné, and Andreas Geiger. 2019. PointFlowNet: Learning Representations for Rigid Motion Estimation From Point Clouds. In *Proceedings of the IEEE/CVF Computer Vision and Pattern Recognition Conference*. 7954–7963.
- [11] Valentina Bianchi, Marco Bassoli, Gianfranco Lombardo, Paolo Fornciari, Monica Mordinini, and Ilaria De Munari. 2019. IoT wearable sensor and deep learning: An integrated approach for personalized human activity recognition in a smart home environment. *IEEE Internet of Things Journal* 6, 5 (2019), 8553–8562.
- [12] Dongjiang Cao, Ruofeng Liu, Hao Li, Shuai Wang, Wenchao Jiang, and Chris Xiaoxuan Lu. 2022. Cross vision-rf gait re-identification with low-cost rgb-d cameras and mmwave radars. *Proceedings of the ACM on Interactive, Mobile, Wearable and Ubiquitous Technologies* 6, 3 (2022), 1–25.
- [13] Z. Cao, G. Hidalgo Martinez, T. Simon, S. Wei, and Y. A. Sheikh. 2019. OpenPose: Realtime Multi-Person 2D Pose Estimation using Part Affinity Fields. *IEEE Transactions on Pattern Analysis and Machine Intelligence* (2019).
- [14] Yixuan Chen, Yunlong Luo, Alex Qi, Miao Miao, and Yihong Qi. 2021. In-cabin Monitoring Based on Millimeter Wave FMCW radar. In *Proceedings of the International Symposium on Antennas, Propagation and EM Theory*. IEEE, 01–03.
- [15] Wencan Cheng and Jong Hwan Ko. 2022. Bi-PointFlowNet: Bidirectional Learning for Point Cloud Based Scene Flow Estimation. In *Proceedings of the European Conference on Computer Vision*. 108–124.
- [16] Kyunghyun Cho, Bart van Merriënboer, Dzmitry Bahdanau, and Yoshua Bengio. 2014. On the Properties of Neural Machine Translation: Encoder–Decoder Approaches. In *Proceedings of the Eighth Workshop on Syntax, Semantics and Structure in Statistical Translation*. 103–111.
- [17] Han Cui and Naim Dahnoun. 2021. High precision human detection and tracking using millimeter-wave radars. *IEEE Aerospace and Electronic Systems Magazine* 36, 1 (2021), 22–32.
- [18] Michael B Del Rosario, Stephen J Redmond, and Nigel H Lovell. 2015. Tracking the evolution of smartphone sensing for monitoring human movement. *Sensors* 15, 8 (2015), 18901–18933.
- [19] Ayush Dewan, Tim Caselitz, Gian Diego Tipaldi, and Wolfram Burgard. 2016. Rigid scene flow for 3D LiDAR scans. In *Proceedings of the IEEE/RSJ International Conference on Intelligent Robots and Systems*. 1765–1770.
- [20] Fangqiang Ding, Andras Palfy, Dariu M. Gavrila, and Chris Xiaoxuan Lu. 2023. Hidden Gems: 4D Radar Scene Flow Learning Using Cross-Modal Supervision. In *Proceedings of the IEEE/CVF Conference on Computer Vision and Pattern Recognition*. 1–10.
- [21] Fangqiang Ding, Zhijun Pan, Yimin Deng, Jianning Deng, and Chris Xiaoxuan Lu. 2022. Self-Supervised Scene Flow Estimation With 4-D Automotive Radar. *IEEE Robotics and Automation Letters* (2022), 1–8.
- [22] Guanting Dong, Yueyi Zhang, Hanlin Li, Xiaoyan Sun, and Zhiwei Xiong. 2022. Exploiting Rigidity Constraints for LiDAR Scene Flow Estimation. In *Proceedings of the IEEE/CVF Computer Vision and Pattern Recognition Conference*. 12776–12785.
- [23] Gianluca Gennarelli and Francesco Soldovieri. 2014. Multipath ghosts in radar imaging: Physical insight and mitigation strategies. *IEEE Journal of Selected Topics in Applied Earth Observations and Remote Sensing* 8, 3 (2014), 1078–1086.
- [24] Zan Gojcic, Or Litany, Andreas Wieser, Leonidas J Guibas, and Tolga Birdal. 2021. Weakly Supervised Learning of Rigid 3D Scene Flow. In *Proceedings of the IEEE/CVF Computer Vision and Pattern Recognition Conference*. 5692–5703.
- [25] Riza Alp Güler, Natalia Neverova, and Iasonas Kokkinos. 2018. Densepose: Dense human pose estimation in the wild. In *Proceedings of the IEEE Conference on Computer Vision and Pattern Recognition*. 7297–7306.
- [26] Souvik Hazra and Avik Santra. 2018. Robust gesture recognition using millimetric-wave radar system. *IEEE Sensors Letters* 2, 4 (2018), 1–4.
- [27] Sepp Hochreiter and Jürgen Schmidhuber. 1997. Long short-term memory. *Neural Computation* 9, 8 (1997), 1735–1780.
- [28] Huang, Shengyu and Gojcic, Zan and Huang, Jiahui and Wieser, Andreas and Schindler, Konrad. 2022. Dynamic 3D Scene Analysis by Point Cloud Accumulation. In *Proceedings of the European Conference on Computer Vision*. 674–690.
- [29] Mariano Jaimez, Mohamed Souiai, Jörg Stückler, Javier Gonzalez-Jimenez, and Daniel Cremers. 2015. Motion cooperation: Smooth piece-wise rigid scene flow from rgb-d images. In *Proceedings of the International Conference on 3D Vision*. IEEE, 64–72.
- [30] Feng Jin, Arindam Sengupta, and Siyang Cao. 2020. mmfall: Fall detection using 4-d mmwave radar and a hybrid variational rnn autoencoder. *IEEE Transactions on Automation Science and Engineering* 19, 2 (2020), 1245–1257.

[31] Philipp Jund, Chris Sweeney, Nichola Abdo, Zhifeng Chen, and Jonathon Shlens. 2021. Scalable scene flow from point clouds in the real world. *IEEE Robotics and Automation Letters* 7, 2 (2021), 1589–1596.

[32] Wolfgang Kabsch. 1976. A solution for the best rotation to relate two sets of vectors. *Acta Crystallographica Section A* 32, 5 (1976), 922–923.

[33] Rajat Khurana and Alok Kumar Singh Kushwaha. 2018. Deep learning approaches for human activity recognition in video surveillance—a survey. In *Proceedings of the International Conference on Secure Cyber Computing and Communication*. IEEE, 542–544.

[34] Sanaz Kianoush, Stefano Savazzi, Federico Vicentini, Vittorio Rampa, and Matteo Giussani. 2016. Device-free RF human body fall detection and localization in industrial workplaces. *IEEE Internet of Things Journal* 4, 2 (2016), 351–362.

[35] Yair Kittenplon, Yonina C Eldar, and Dan Raviv. 2021. FlowStep3D: Model Unrolling for Self-Supervised Scene Flow Estimation. In *Proceedings of the IEEE/CVF Computer Vision and Pattern Recognition Conference*. 4114–4123.

[36] Hao Kong, Xiangyu Xu, Jiadi Yu, Qilin Chen, Chenguang Ma, Yingying Chen, Yi-Chao Chen, and Linghe Kong. 2022. m3track: mmwave-based multi-user 3d posture tracking. In *Proceedings of the 20th Annual International Conference on Mobile Systems, Applications and Services*. 491–503.

[37] Ryanne JM Lemmens, Yvonne JM Janssen-Potten, Annick AA Timmermans, Rob JEM Smeets, and Henk AM Seelen. 2015. Recognizing complex upper extremity activities using body worn sensors. *PLoS one* 10, 3 (2015), e0118642.

[38] Ruibo Li, Chi Zhang, Guosheng Lin, Zhe Wang, and Chunhua Shen. 2022. RigidFlow: Self-Supervised Scene Flow Learning on Point Clouds by Local Rigidity Prior. In *Proceedings of the IEEE/CVF Computer Vision and Pattern Recognition Conference*. 16959–16968.

[39] Xueqian Li, Jhony Kaesemel Pontes, and Simon Lucey. 2021. Neural scene flow prior. *Advances in Neural Information Processing System* 34 (2021), 7838–7851.

[40] Jaime Lien, Nicholas Gillian, M Emre Karagozler, Patrick Amihood, Carsten Schwesig, Erik Olson, Hakim Raja, and Ivan Poupyrev. 2016. Soli: Ubiquitous gesture sensing with millimeter wave radar. *ACM Transactions on Graphics* 35, 4 (2016), 1–19.

[41] Haipeng Liu, Anfu Zhou, Zihe Dong, Yuyang Sun, Jiahe Zhang, Liang Liu, Huadong Ma, Jianhua Liu, and Ning Yang. 2021. M-gesture: Person-independent real-time in-air gesture recognition using commodity millimeter wave radar. *IEEE Internet of Things Journal* 9, 5 (2021), 3397–3415.

[42] Peng Liu, Michael Reale, and Lijun Yin. 2012. 3d head pose estimation based on scene flow and generic head model. In *Proceedings of the IEEE International Conference on Multimedia and Expo*. IEEE, 794–799.

[43] Xingyu Liu, Charles R Qi, and Leonidas J Guibas. 2019. FlowNet3D: Learning Scene Flow in 3D Point Clouds. In *Proceedings of the IEEE/CVF Computer Vision and Pattern Recognition Conference*. 529–537.

[44] Wenjie Lv, Wangdong He, Xipeng Lin, and Jungang Miao. 2021. Non-contact monitoring of human vital signs using FMCW millimeter wave radar in the 120 GHz band. *Sensors* 21, 8 (2021), 2732.

[45] Balmukund Mishra, Deepak Garg, Pratik Narang, and Vipul Mishra. 2020. Drone-surveillance for search and rescue in natural disaster. *Computer Communications* 156 (2020), 1–10.

[46] Himangi Mittal, Brian Okorn, and David Held. 2020. Just go with the flow: Self-supervised scene flow estimation. In *Proceedings of the IEEE/CVF Computer Vision and Pattern Recognition Conference*. 11177–11185.

[47] Subhas Chandra Mukhopadhyay. 2014. Wearable sensors for human activity monitoring: A review. *IEEE Sensors Journal* 15, 3 (2014), 1321–1330.

[48] Manoranjan Paul, Shah ME Haque, and Subrata Chakraborty. 2013. Human detection in surveillance videos and its applications—a review. *EURASIP Journal on Advances in Signal Processing* 2013, 1 (2013), 1–16.

[49] Jhony Kaesemel Pontes, James Hays, and Simon Lucey. 2020. Scene flow from point clouds with or without learning. In *Proceedings of the International Conference on 3D Vision*. 261–270.

[50] Gilles Puy, Alexandre Boulch, and Renaud Marlet. 2020. Flot: Scene flow on point clouds guided by optimal transport. In *Proceedings of the European Conference on Computer Vision*. 527–544.

[51] Charles Ruizhongtai Qi, Li Yi, Hao Su, and Leonidas J Guibas. 2017. Pointnet++: Deep hierarchical feature learning on point sets in a metric space. *Advances in Neural Information Processing Systems* 30 (2017).

[52] Yili Ren, Zi Wang, Yichao Wang, Sheng Tan, Yingying Chen, and Jie Yang. 2022. Gopose: 3d human pose estimation using wifi. *Proceedings of the ACM on Interactive, Mobile, Wearable and Ubiquitous Technologies* 6, 2 (2022), 1–25.

[53] Louis L Scharf and Cédric Demeure. 1991. *Statistical signal processing: detection, estimation, and time series analysis*. Prentice Hall.

[54] Chris Schwarz, Hunza Zainab, Soura Dasgupta, and Justin Kahl. 2021. Heartbeat measurement with millimeter wave radar in the driving environment. In *Proceedings of the IEEE Radar Conference*. IEEE, 1–6.

[55] Xiangbo Shu, Liyan Zhang, Yunlian Sun, and Jinhui Tang. 2020. Host-parasite: Graph LSTM-in-LSTM for group activity recognition. *IEEE Transactions on Neural Networks and Learning Systems* 32, 2 (2020), 663–674.

[56] Akash Deep Singh, Sandeep Singh Sandha, Luis Garcia, and Mani Srivastava. 2019. Radhar: Human activity recognition from point clouds generated through a millimeter-wave radar. In *Proceedings of the 3rd ACM Workshop on Millimeter-wave Networks and Sensing Systems*. 51–56.

[57] Rameesha Tariq, Maham Rahim, Nimra Aslam, Narmeen Bawany, and Ummay Faseeha. 2018. Dronaid: A smart human detection drone for rescue. In *Proceedings of the International Conference on Smart Cities: Improving Quality of Life Using ICT & IoT*. 33–37.

[58] William Taylor, Syed Aziz Shah, Kia Dashtipour, Adnan Zahid, Qammer H Abbasi, and Muhammad Ali Imran. 2020. An intelligent non-invasive real-time human activity recognition system for next-generation healthcare. *Sensors* 20, 9 (2020), 2653.

[59] Yonglong Tian, Guang-He Lee, Hao He, Chen-Yu Hsu, and Dina Katabi. 2018. RF-based fall monitoring using convolutional neural networks. *Proceedings of the ACM on Interactive, Mobile, Wearable and Ubiquitous Technologies* 2, 3 (2018), 1–24.

[60] Shih-Pang Tseng, Bo-Rong Li, Jun-Long Pan, and Chia-Ju Lin. 2014. An application of Internet of things with motion sensing on smart house. In *Proceedings of the International Conference on Orange Technologies*. IEEE, 65–68.

[61] Bo Wang, Liang Guo, Hao Zhang, and Yong-Xin Guo. 2020. A millimetre-wave radar-based fall detection method using line kernel convolutional neural network. *IEEE Sensors Journal* 20, 22 (2020), 13364–13370.

[62] Chuyu Wang, Jian Liu, Yingying Chen, Lei Xie, Hong Bo Liu, and Sanclu Lu. 2018. RF-kinect: A wearable RFID-based approach towards 3D body movement tracking. *Proceedings of the ACM on Interactive, Mobile, Wearable and Ubiquitous Technologies* 2, 1 (2018), 1–28.

[63] Haiyan Wang, Jiahao Pang, Muhammad A Lodhi, Yingli Tian, and Dong Tian. 2021. FESTA: Flow Estimation via Spatial-Temporal Attention for Scene Point Clouds. In *Proceedings of the IEEE/CVF Computer Vision and Pattern Recognition Conference*. 14173–14182.

[64] Pichao Wang, Wanqing Li, Zhimin Gao, Yuyao Zhang, Chang Tang, and Philip Ogunbona. 2017. Scene flow to action map: A new representation for rgb-d based action recognition with convolutional neural networks. In *Proceedings of the IEEE Conference on Computer Vision and Pattern*

Recognition. 595–604.

[65] Shuai Wang, Dongjiang Cao, Ruofeng Liu, Wenchoao Jiang, Tianshun Yao, and Chris Xiaoxuan Lu. 2023. Human Parsing with Joint Learning for Dynamic mmWave Radar Point Cloud. *Proceedings of the ACM on Interactive, Mobile, Wearable and Ubiquitous Technologies* 7, 1 (2023), 1–22.

[66] Yuheng Wang, Haipeng Liu, Kening Cui, Anfu Zhou, Wensheng Li, and Huadong Ma. 2021. m-activity: Accurate and real-time human activity recognition via millimeter wave radar. In *Proceedings of the IEEE International Conference on Acoustics, Speech and Signal Processing*. 8298–8302.

[67] Yong Wang, Wen Wang, Mu Zhou, Aihu Ren, and Zengshan Tian. 2020. Remote monitoring of human vital signs based on 77-GHz mm-wave FMCW radar. *Sensors* 20, 10 (2020), 2999.

[68] Zirui Wang, Shuda Li, Henry Howard-Jenkins, Victor Prisacariu, and Min Chen. 2020. Flownet3d++: Geometric losses for deep scene flow estimation. In *Proceedings of the IEEE/CVF Winter Conference on Applications of Computer Vision*. 91–98.

[69] Yi Wei, Ziyi Wang, Yongming Rao, Jiwen Lu, and Jie Zhou. 2021. PV-RAFT: point-voxel correlation fields for scene flow estimation of point clouds. In *Proceedings of the IEEE/CVF Computer Vision and Pattern Recognition Conference*. 6954–6963.

[70] John M Weiss. 2009. Continuous-wave stepped-frequency radar for target ranging and motion detection. In *Proceedings of MICS symposium*.

[71] Wenzxuan Wu, Zhi Yuan Wang, Zhuwen Li, Wei Liu, and Li Fuxin. 2020. PointPWC-Net: Cost Volume on Point Clouds for (Self-) Supervised Scene Flow Estimation. In *Proceedings of the European Conference on Computer Vision*. 88–107.

[72] Hongfei Xue, Qiming Cao, Yan Ju, Haochen Hu, Haoyu Wang, Aidong Zhang, and Lu Su. 2022. M4esh: mmWave-Based 3D Human Mesh Construction for Multiple Subjects. In *Proceedings of the 20th ACM Conference on Embedded Networked Sensor Systems*. 391–406.

[73] Hongfei Xue, Yan Ju, Chenglin Miao, Yijiang Wang, Shiyang Wang, Aidong Zhang, and Lu Su. 2021. mmMesh: towards 3D real-time dynamic human mesh construction using millimeter-wave. In *Proceedings of the 19th Annual International Conference on Mobile Systems, Applications, and Services*. 269–282.

[74] Peijun Zhao, Chris Xiaoxuan Lu, Bing Wang, Niki Trigoni, and Andrew Markham. 2023. CubeLearn: End-to-end learning for human motion recognition from raw mmWave radar signals. *IEEE Internet of Things Journal* (2023).

[75] Peijun Zhao, Chris Xiaoxuan Lu, Jianan Wang, Changhao Chen, Wei Wang, Niki Trigoni, and Andrew Markham. 2019. mid: Tracking and identifying people with millimeter wave radar. In *Proceedings of the International Conference on Distributed Computing in Sensor Systems*. 33–40.

[76] Peijun Zhao, Chris Xiaoxuan Lu, Jianan Wang, Changhao Chen, Wei Wang, Niki Trigoni, and Andrew Markham. 2021. Human tracking and identification through a millimeter wave radar. *Ad Hoc Networks* 116 (2021), 102475.